

A Study of the Long-term Spectral Variations of 3C 66A Observed with the *Fermi* and Kanata Telescopes

Ryosuke ITOH^{1,2}, Yasushi FUKAZAWA^{1,3}, James CHIANG⁴, Yoshitaka HANABATA¹, Masaaki HAYASHIDA^{4,5},
Katsuhiro HAYASHI¹, Tsunefumi MIZUNO⁶, Masanori OHNO¹, Takashi OHSUGI¹, Jeremy S. PERKINS^{7,8,9,10},
Silvia RAINÒ^{11,12}, Luis C. REYES¹³, Hiromitsu TAKAHASHI¹, Yasuyuki TANAKA⁶, Gino TOSTI^{14,15},
Hiroschi AKITAYA⁶, Akira ARAI¹⁶, Masaru KINO¹⁷, Yuki IKEJIRI¹, Koji S. KAWABATA⁶, Tomoyuki KOMATSU¹,
Kiyoshi SAKIMOTO¹, Mahito SASADA¹⁸, Shuji SATO¹⁷, Makoto UEMURA⁶, Takahiro UI¹, Masayuki YAMANAKA¹⁹ and
Michitoshi YOSHIDA⁶

¹Department of Physical Sciences, Hiroshima University, Higashi-Hiroshima, Hiroshima 739-8526, Japan

²email: itoh@hep01.hepl.hiroshima-u.ac.jp

³email: fukazawa@hep01.hepl.hiroshima-u.ac.jp

⁴W. W. Hansen Experimental Physics Laboratory, Kavli Institute for Particle Astrophysics and Cosmology, Department of Physics and SLAC
National Accelerator Laboratory, Stanford University, Stanford, CA 94305, USA

⁵Department of Astronomy, Graduate School of Science, Kyoto University, Sakyo-ku, Kyoto 606-8502, Japan

⁶Hiroshima Astrophysical Science Center, Hiroshima University, Higashi-Hiroshima, Hiroshima 739-8526, Japan

⁷NASA Goddard Space Flight Center, Greenbelt, MD 20771, USA

⁸Department of Physics and Center for Space Sciences and Technology, University of Maryland Baltimore County, Baltimore, MD 21250, USA

⁹Center for Research and Exploration in Space Science and Technology (CRESSST) and NASA Goddard Space Flight Center, Greenbelt, MD
20771, USA

¹⁰Harvard-Smithsonian Center for Astrophysics, Cambridge, MA 02138, USA

¹¹Dipartimento di Fisica “M. Merlin” dell’Università e del Politecnico di Bari, I-70126 Bari, Italy

¹²Istituto Nazionale di Fisica Nucleare, Sezione di Bari, 70126 Bari, Italy

¹³Department of Physics, California Polytechnic State University, San Luis Obispo, CA 93401, USA

¹⁴Istituto Nazionale di Fisica Nucleare, Sezione di Perugia, I-06123 Perugia, Italy

¹⁵Dipartimento di Fisica, Università degli Studi di Perugia, I-06123 Perugia, Italy

¹⁶Department of Physics, Kyoto Sangyo University, Kyoto, Japan

¹⁷Department of Physics and Astrophysics, Nagoya University, Chikusa-ku Nagoya 464-8602, Japan

¹⁸Department of Physics, Graduate School of Science, Kyoto University, Kyoto, Japan

¹⁹Kwasan Observatory, Kyoto University, Kyoto, Japan

(Received ; accepted)

Abstract

3C 66A is an intermediate-frequency-peaked BL Lac object detected by the Large Area Telescope onboard the *Fermi* Gamma-ray Space Telescope. We present a study of the long-term variations of this blazar seen over ~ 2 years at GeV energies with *Fermi* and in the optical (flux and polarization) and near infrared with the Kanata telescope. In 2008, the first year of the study, we find a correlation between the gamma-ray flux and the measurements taken with the Kanata telescope. This is in contrast to the later measurements performed during 2009–2010 which show only a weak correlation along with a gradual increase of the optical flux. We calculate an external seed photon energy density assuming that the gamma-ray emission is due to external Compton scattering. The energy density of the external photons is found to be higher by a factor of two in 2008 compared to 2009–2010. We conclude that the different behaviors observed between the first year and the later years might be explained by postulating two different emission components.

Key words: galaxies: BL Lacertae objects: general₁ — gamma rays: observations₂

1. Introduction

Blazars are highly variable active galactic nuclei (AGN) detected at all wavelengths from radio to gamma rays. They have strong relativistic jets aligned with the observer’s line of sight and are apparently bright due to relativistic beaming. Their emission typically consists of two spectral components. The first, highly polarized, one is attributed to synchrotron radiation from relativistic electrons and is emitted at lower energies (typically radio to UV). The other, higher energy, com-

ponent (typically X-ray to TeV), is not fully understood. The most plausible scenario is that the emission is due to inverse Compton scattering off some combination of synchrotron and external photons.

3C 66A is one of the most famous TeV blazars, and is classified as an intermediate-frequency-peaked BL Lac object (IBL; Schlegel et al. 1998; Abdo et al. 2010a). Its low-energy component extends from radio to soft X-rays with a peak in the optical band (Abdo et al. 2010a). Most TeV BL Lac objects are classified as HBL (high-frequency-peaked BL Lac), and therefore

3C 66A, as an IBL, is a rare and valuable source which can be used to study the emission mechanisms of high-energy gamma-rays. The high-energy component located in the MeV to TeV gamma-ray band, can be explained by a Synchrotron Self-Compton (SSC) plus External Compton (EC) model (Abdo et al. 2011, and references therein, referred to as ‘‘Paper I’’). 3C 66A is listed as 2FGL J0222.6+4302 in the *Fermi* Large Area Telescope (LAT) second source catalog (Nolan et al. 2012). Due to a lack of strong emission lines in the optical band, the redshift is uncertain. Miller et al. (1978) reported a redshift $z = 0.444$ based on a detection of the Mg II line. However, as pointed out by Bramel et al. (2005), this redshift is unreliable and should be reported as $z = 0.11 \sim 0.444$ because it was determined by only a single weak line. The redshift uncertainty prevents a definite correction of the TeV gamma-ray absorption by the Extragalactic Background Light (EBL). Thus, the true spectrum is not well known and the emission mechanism in the TeV gamma-ray band is not yet understood. Thus, multiwavelength observations are an extremely powerful tool to probe the emission mechanism.

The launch of the *Fermi Gamma-ray Space Telescope* started a new era of multiwavelength monitoring observations of AGN. In particular, the all-sky monitoring capability of the *Fermi*-LAT Telescope has prompted extensive simultaneous gamma-ray and optical observing campaigns. These are important since correlation studies between the GeV gamma-ray and optical bands of IBLs provide information on the source electron population. Optical polarization measurements are particularly important since they can probe jet structures. In this paper, we report a correlation study of the GeV gamma-ray and optical emission of 3C 66A, based on simultaneous observations by the Large Area Telescope onboard the *Fermi Gamma-ray Space Telescope* and the Kanata optical telescope. We assume a flat Λ CDM cosmology with $H_0 = 71 \text{ km s}^{-1} \text{ Mpc}^{-1}$ and $\Omega_m = 0.27$ (Wright, E. L. 2006).

2. Observations and Results

2.1. *Fermi* observations and Data analysis

The LAT is the main instrument onboard the *Fermi Gamma-ray Space Telescope*. The LAT is an electron-positron pair production detector which is sensitive to gamma rays with energies from 20 MeV to $> 300 \text{ GeV}$. The LAT observes the whole sky every 3 hours with a large effective area of 8000 cm^2 at 1 GeV, a wide field of view of 2.4 sr, and a single photon angular resolution (68% containment radius) of 0.1° at 10 GeV. Details of the LAT instrument are described in Atwood et al. (2009). The data used in this analysis were taken between 2008 August and 2010 February almost entirely in sky survey mode. The data were analyzed using the standard *Fermi* analysis software (`Science Tools`, version v9r15, IRFs P6_V3¹). In order to limit residual contamination of charged-particle backgrounds, only ‘‘Diffuse’’ class event data above 100 MeV were selected. ‘‘Diffuse’’ class events are highly likely to be photons. We also restricted our analysis to events with zenith angles $< 105^\circ$ and rocking angles of the LAT $< 52^\circ$ to limit

the contamination by gamma rays from the Earth’s limb. We performed an *Unbinned Likelihood* analysis to calculate the gamma-ray spectrum and flux of 3C 66A, using the `gtlike` package in the `Science Tools`. An area of 15° around 3C 66A was selected as a region of interest (ROI) for this analysis. We constructed a model of the ROI that includes a point source at the position of 3C 66A (R.A. = 35.662° , Dec. = 43.036° , J2000), the Galactic diffuse emission component (`gll_iem_v02.fit`) and the isotropic diffuse emission component (`isotropic_iem_v02.txt`, this is the sum of the extragalactic diffuse gamma-ray and the residual charged particle background). There are also six bright (Test Statistic > 100)² point sources within 15° of 3C 66A which were included in the model, as shown in Figure 1 and Table 1. The other sources with a TS values of < 100 in *Fermi* LAT first source catalog (Abdo et al. 2010d) are not included in the model. It is necessary to account for the emission from the pulsar PSR J0218+4232, located at 0.96° from 3C 66A. Due to the small point spread function of the LAT (Atwood et al. 2009), we can separate the emission from the pulsar from the emission from 3C 66A and obtain an accurate measurement of the GeV gamma-ray flux of 3C 66A without a risk of contamination from the pulsar. The gamma-ray emission from PSR J0218+4232, can be represented by the following pulsar super exponential cutoff (`PLSuperExpCutoff`) function.

$$\frac{dN}{dE} = N_0 \left(\frac{E}{E_0} \right)^{-\gamma} \exp \left(-\frac{E}{E_c} \right) \quad (1)$$

We fixed γ , E_0 , and E_c to the values found in Abdo et al. (2010b): $\gamma = 2.02$, $E_0 = 1 \text{ GeV}$ and $E_c = 5.1 \text{ GeV}$.

We verified that the flux of PSR J0218+4232 is stable by creating a light curve with 50 day time bins, and confirmed that the flux is statistically constant within the errors. A χ^2 test for a constant fit to the light curve of PSR J0218+4232 yielded a $\chi^2/\text{d.o.f} = 4.008/7$. Hereafter, we fixed the model parameters of the spectral shape of PSR J0218+4232 to those listed above.

Table 1. Background point sources included in the model.

Source name	Separation from 3C 66A [deg]
1FGL J0136.5+3905	9.5
1FGL J0137.0+4751	9.3
1FGL J0221.0+3555	7.1
1FGL J0237.9+2848	14.6
1FGL J0319.7+4130	10.6
PSR J0218+4232	0.96

We modeled the spectrum of 3C 66A as a power-law:

$$\frac{dN}{dE} = N_0 \left(\frac{E}{E_0} \right)^{-\gamma} \quad (2)$$

where N_0 is the normalization at energy $E_0 = 100 \text{ MeV}$ and γ is the photon index. The same model was used for the other point sources in the ROI, except for PSR J0218+4232. The integrated photon flux between 100 MeV and 100 GeV is cal-

¹ http://fermi.gsfc.nasa.gov/ssc/data/analysis/documentation/Cicerone/Cicerone_LAT_IRFs/IRF_overview.html

² The Test Statistic (TS) is defined as $\text{TS} = -2(\log L_0 - \log L_1)$ with L_0 the likelihood of the Null hypothesis model as compared to the likelihood of a competitive model L_1

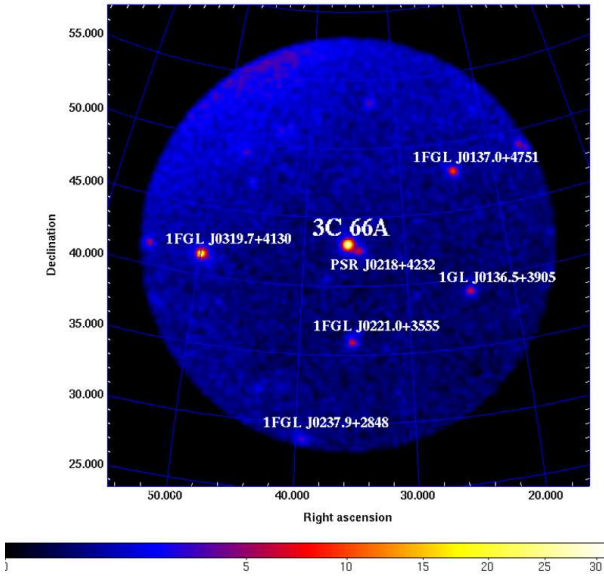


Fig. 1. Smoothed count map of the 3C 66A region as seen by *Fermi*-LAT between 2008 August and 2010 February with data above 1 GeV.

culated by integrating equation 2. In the source model for the likelihood analysis, the spectral indices of the background sources were fixed to their catalog values while their normalizations were left free.

Figure 2 shows how the flux and photon index of 3C 66A varies with time in the 100 MeV to 100 GeV energy band calculated by performing a likelihood analysis in 5-day time intervals. Data points which have small TS values (< 10) are designated by arrows and indicate 90% C.L. upper limits. Two flares are evident in the light curve, one around MJD 54750 (hereafter “flare 1”), and the other one around MJD 54960 (“flare 2”). Flare 2 is not considered in this paper because simultaneous optical data are not available due to the proximity of 3C 66A to the Sun during the flare. The maximum flux during flare 1, which is also discussed in Paper I, is $5 \times 10^{-7} \text{ ph cm}^{-2} \text{ s}^{-1}$ from 0.1–100 GeV. Except during these flares, the flux of 3C 66A is around $\sim 2 \times 10^{-7} \text{ ph cm}^{-2} \text{ s}^{-1}$ (0.1–100 GeV), as reported in Paper I. On the other hand, the photon index does not change significantly (a χ^2 test with a constant fit gives a $\chi^2/\text{d.o.f} = 138.5/121$) and no clear correlation with the flux is seen. Figure 3 illustrates a trend; the spectrum is softer when the flux is higher. However, this could be parameter coupling since there is a mathematical correlation between the integral flux and index; the integral flux is obtained from integrating equation 2. In addition, the sensitivity of the LAT is greater for harder spectrum objects. This correlation can also be caused by observational bias, so we cannot conclude that this correlation is significant. This is consistent with the findings of Abdo et al. (2010g), who state that intermediate synchrotron peaked blazars (ISPs) in general show only a small change of photon index (< 0.2) with flux variations.

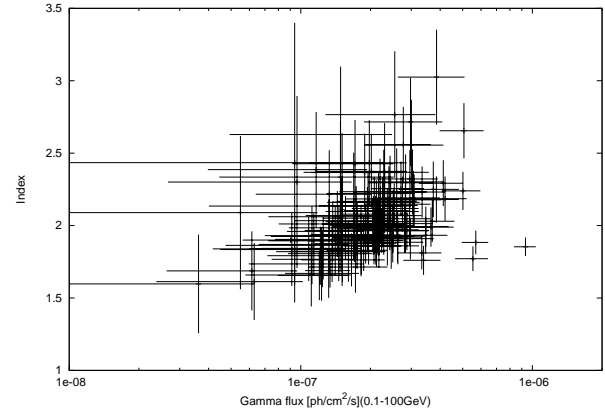


Fig. 3. GeV gamma-ray flux vs. photon index.

2.2. Kanata Telescope Observations and Optical properties

We performed *V*, *J*, *Ks*-band photometry and polarimetry observations of 3C 66A from July 2008 to February 2010, using the TRISPEC instrument installed on the 1.5m Kanata telescope located at the Higashi-Hiroshima Observatory in Japan. The TRISPEC consists of a CCD and two InSb arrays, enabling photopolarimetric observations in one optical and two NIR bands simultaneously (Watanabe et al. 2005).

We obtained 278 photometry and 208 polarimetry observations in the *V* band, 180 photometry observations in the *J* band, and 77 photometry observations in the *Ks* band. Each observing sequence consisted of successive exposures at four position angles of a half-wave plate; 0° , 45° , 22.5° , and 67.5° . The data reduction involved standard CCD photometry procedures; aperture photometry using APPHOT packaged in PYRAF^{3 4}, and differential photometry with a comparison star taken in the same frame of 3C 66A. The position of the comparison star is R.A. = $02^{\text{h}}22^{\text{m}}55.12^{\text{s}}$ and Dec = $+43^\circ03'15.5''$ (J2000), and its magnitudes are $V = 12.809$, $J = 12.371$, $Ks = 12.282$ (Gonzalez-Perez et al. 2001, Cutri et al. 2003). The data have been corrected for Galactic extinction using $A(V) = 0.274$ and $A(J) = 0.076$. We confirmed that the instrumental polarization was smaller than 0.1% in the *V* band, using unpolarized standard stars and thus applied no correction for it. The polarization angle (PA) is defined in the standard manner (measured from north to east), by calibrations with polarized stars, HD19820 and HD25443 (Wolff et al. 1996). Because the PA has an ambiguity of $\pm 180^\circ \times n$ (where n is an integer), we selected n which gives the least angle difference from previous measurements, assuming that the PA would change smoothly.

Figure 4 shows how the optical and NIR flux and polarization change with time. The GeV gamma-ray light curve from Figure 2 is reproduced in panel 1 for comparison. Several polarization and flux states are seen in the optical data. Based on the optical flux and polarization degree (PD), we define four periods; MJD 54705–54830 (hereafter “period 1”), MJD 54831–55047 (“period 2”), MJD 55048–55150 (“period 3”) and MJD 55151–55220 (“period 4”). We collect the properties

³ PYRAF is a product of the Space Telescope Science Institute, which is operated by AURA for NASA.

⁴ http://www.stsci.edu/institute/software_hardware/pyraf

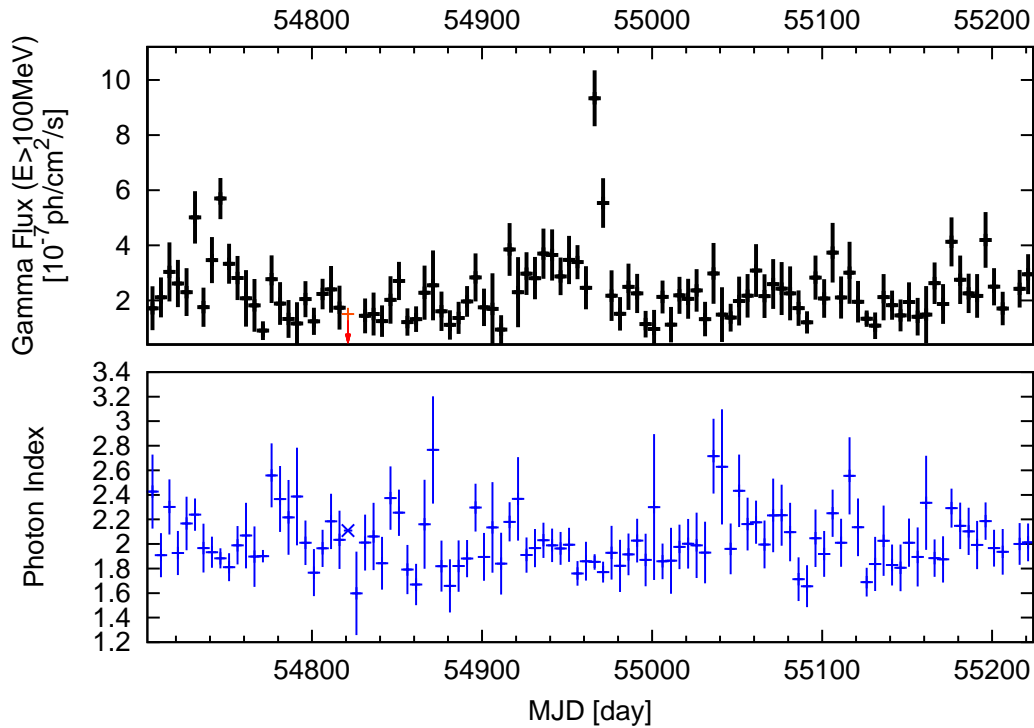


Fig. 2. GeV Gamma-ray light curve of 3C 66A measured by the *Fermi* LAT from MJD 54683 to 55232 (2008-08-04 to 2010-02-04). One bin corresponds to 5 days. The upper panel shows the integral photon flux from 100MeV–100GeV, and the lower panel shows the photon index. Bins with TS values smaller than 10 are indicated by arrows and are 90% C.L. upper limits.

of variability for each period. In period 1, both the gamma-ray flux at 20 GeV and the optical V band flux (F_{G1}, F_{V1}) are low at an average of $F_{G1} = (3.5 \pm 1.6) \times 10^{-11} \text{ erg cm}^{-2} \text{ s}^{-1}$, $F_{V1} = (3.2 \pm 0.9) \times 10^{-11} \text{ erg cm}^{-2} \text{ s}^{-1}$ respectively, with the exception of the flare 1. During period 1 the optical properties vary violently and the gamma-ray flux is well correlated with the optical flux, color, and polarization degree.

On MJD 54830 (the beginning of period 2), the optical flux suddenly increased and a high-optical-flux state began. The optical coverage during parts of period 2 are incomplete because 3C 66A was located near the Sun. Thus correlation studies during this time are problematic. The polarization degree became relatively low (its average value in periods 1 and 2 are $PD_1 = 11.9\%$ and $PD_2 = 6.6\%$, respectively) and the PA is also constant. From MJD 54835 to MJD 54850, the PA changed by almost 180° in 2 weeks. Such a rotation of PA is similar to that found for BL Lac and 3C 279 (Marscher et al. 2008; Abdo et al. 2010c). Figure 5 shows the variation of PA and Stokes parameters Q and U from MJD 54835 to MJD 54850. The variation on the QU plane implies rotation, but it could be due to random motion around the origin of the QU plane. Because of the aforementioned observation sparseness, we cannot discuss this behavior further.

In period 3, continuous optical observations are available, and the PD became relatively high (the average value in period 3 is $PD_3 = 12.4\%$).

In period 4, the PD became lower (the average value is

$PD_4 = 8.0\%$) and the color reddened. The optical flux was higher than in the other periods but the gamma-ray flux ($F_{G4} = (3.8 \pm 1.6) \times 10^{-11} \text{ erg cm}^{-2} \text{ s}^{-1}$) was similar to that in other periods. A weak flare in the optical band was seen on MJD 55190, associated with a decrease of the PD and a temporary shift of the PA by $\sim 40^\circ$.

2.3. Correlation Studies

Correlations between the various gamma-ray and optical properties can be quantified by calculating the discrete correlation function (DCF) (Edelson & Krolik 1998). Since the gamma-ray flux is averaged over 5-day intervals, it was necessary to also average the optical data. The significance of the correlation (95% C.L.) was tested using the Student's t-test. A test statistic for the t-test (TS_t) was calculated as follows,

$$TS_t = \frac{DCF}{\sqrt{1 - DCF^2}} \times \sqrt{n - 2} \quad (3)$$

where DCF is the DCF value and n is the number of degrees of freedom. The DCF value for zero time lag corresponds to the correlation coefficient. If the TS_t value is larger than the critical values of the t-distribution for a significance level of $\alpha = 0.95$ against the null hypothesis and the DCF value is larger than 0.5, then the correlation is considered significant.

In Table 2, we summarize the correlation coefficients and t-test results for each combination of observed values. Only period 1 shows a possible correlation between the gamma-ray and optical flux. This correlation can be seen in Fig. 6 which

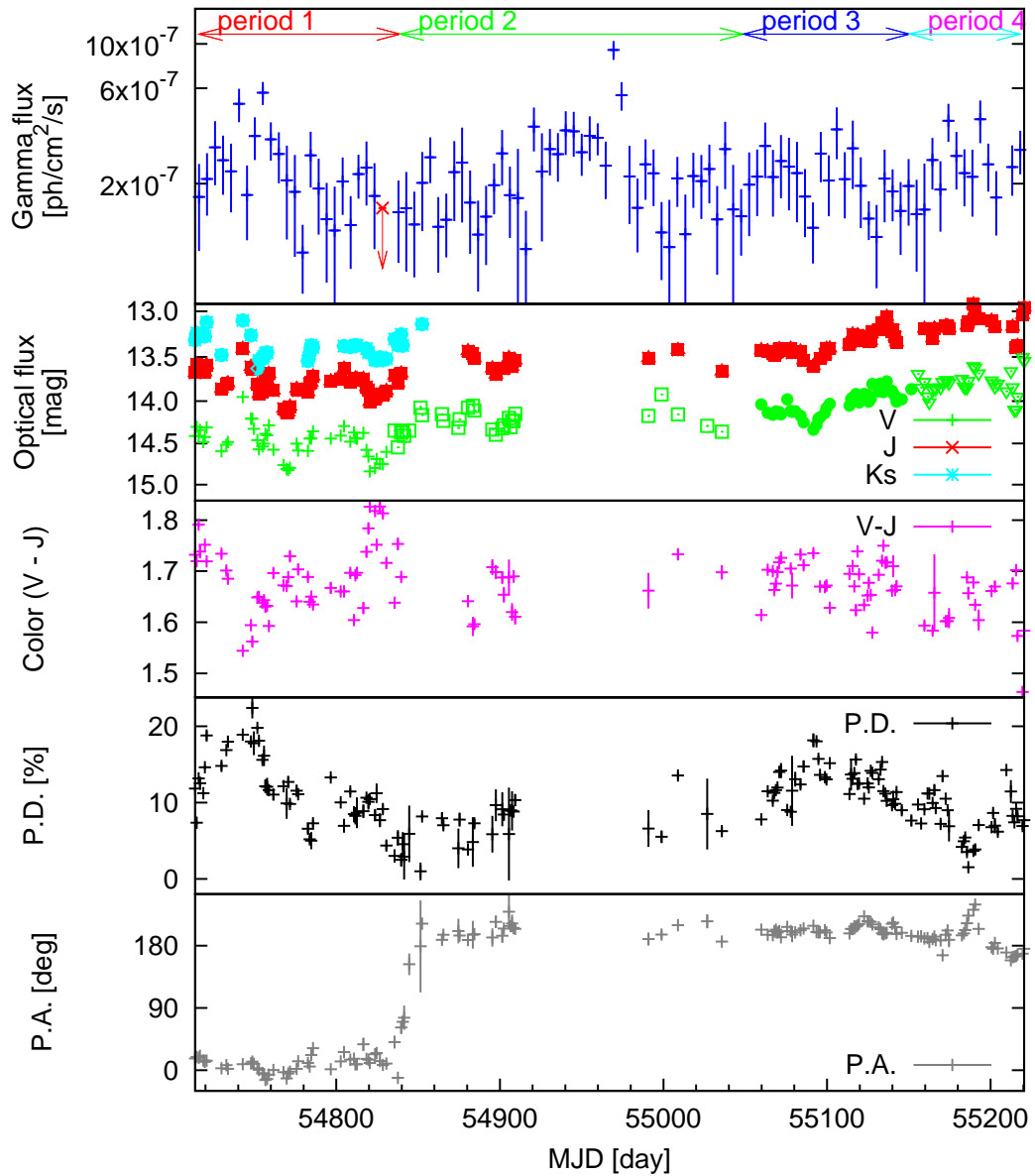


Fig. 4. Optical flux and polarization of 3C 66A plotted versus time as measured by the Kanata telescope. The Gamma-ray light curve (100MeV–100GeV) is shown in the top panel for comparison. Bins with TS values smaller than 10 are indicated by arrows and are 90% C.L. upper limits. The second panel is the optical V, J and Ks-band flux in units of magnitude. The third panel shows the optical color index (V band - J band). The fourth panel is the V-band polarization degree (PD) and the bottom panel is the polarization angle (PA).

plots the gamma-ray flux versus the optical flux and designates each period with different colors. The correlation in period 1 reported here is also suggested in Fig. 6 and is consistent with previous measurements (Paper I). The correlation between the optical flux and optical polarization degree at zero lag is not significant in any of the periods. Fig. 10 shows the DCF of the PD against the optical flux for each period. The PD variation in period 1 seems to correlate with the optical flux with some time offsets; the extrema on MJD 54750, 54770, 54830, and 55190, are seen in both the optical flux and PD. It can be seen that

the PD correlated with the optical flux with a 5–7 day delay in period 1 and anti-correlated with a ~ 6 day precedence in period 4. Such an anti-correlation between the optical flux and polarization has been found for other blazars with the Kanata telescope (Ikejiri et al. 2011). The optical polarization shows a correlation with the gamma-ray flux in period 1 (Fig. 8), and with the optical color in periods 1, 2, and 4 (Fig. 7, this is known as a bluer-when-brighter trend).

We note several differences in the correlation trends between the four periods. Fig.6 shows that the optical flux is different

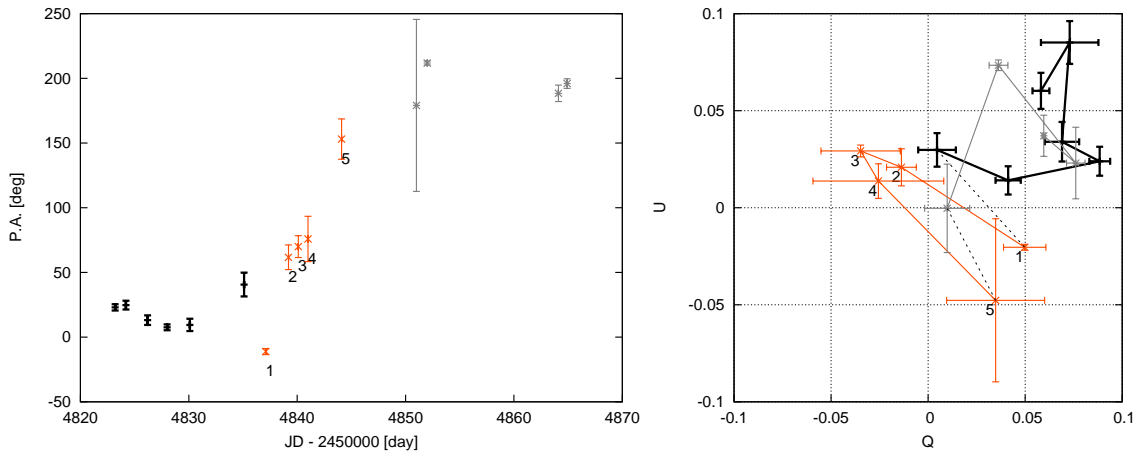


Fig. 5. The left plot shows the PA versus time for the period around MJD 54830 and the right plot shows the QU-plane for this same time period. The plots are color and number coded so that specific time periods can be referenced.

in different periods by a factor of 3–4 for the same gamma-ray flux. If the origin of the gamma-ray emission is identical to that of the optical emission and the environment of the emission region is the same, the gamma-ray and optical fluxes should change together.

The PD is systematically different among the four periods (Fig. 7). This behavior is due to a slow change of the PD in the long-term variable component. This trend is similar to that found for 3C 454.3 (Sasada et al. 2010). An anti-correlation between the optical flux and PD is seen during periods 3 and 4, and this could be due to such a long-term variation. A bluer-when-brighter trend is seen within each period, as well as between periods 1 and 2 and between periods 3 and 4 (Fig. 9). This is due to the long-term change of color as reported for 3C 454.3 (Sasada et al. 2010). However, the color-flux relation is systematically different between periods 1–2 and 3–4; the color in periods 3–4 is redder than that in periods 1–2. As a result, the correlation is weak over the full data set. Assuming a new emission region appeared in periods 3–4, the correlation would not be significant. These observations imply at least two components with different variability timescales in the optical band.

3. Discussion

Many FSRQs, such as PKS 1510-089 (Abdo et al. 2010e), 3C 279 (Abdo et al. 2010c), PKS 1502+106 (Abdo et al. 2010f), and 3C 454.3 (Striani et al. 2010), exhibit clear correlations between their gamma-ray and optical properties. Additionally, their broad-band spectral energy distributions (SED) are better explained by SSC+EC models than SSC models (Abdo et al. 2010a). These prior measurements indicate that the radiation region of gamma-rays is the same as that of the optical emission for FSRQs and LBLs. From our observations, 3C 66A presents two different behaviors: one with a correlation between the gamma-ray and the optical bands, and another uncorrelated one. The correlation in period 1 in 2008 was also reported in Paper I, and, for the first time during the *Fermi* era, the gamma-ray emission of this IBL can be explained by

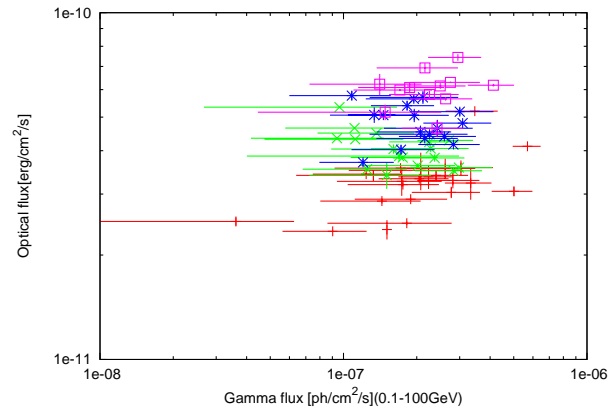


Fig. 6. Gamma-ray flux vs. Optical V band flux. Colors indicate four periods; red: period 1 (MJD 54706–54831), green: period 2 (MJD 54831–55047), blue: period 3 (MJD 55047–55151), and pink: period 4 (MJD 55151–55220).

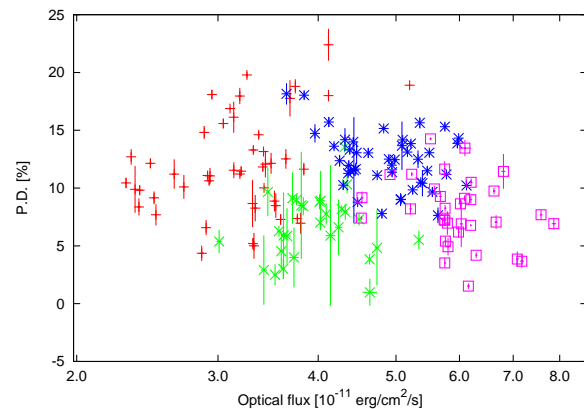


Fig. 7. Optical V band flux vs. optical polarization degree (PD). Colors are the same as those of Fig. 6.

a SSC+EC model (prior measurements of the IBL W Comae

Table 2. Correlation coefficients. The significance of the correlation was tested using the Student's t-test. Correlation coefficients whose significance is within the 95% confidence interval are marked with an asterisk.

	Period 1	Period 2	Period 3	Period 4
Gamma-ray vs V band	$0.53 \pm 0.22^*$	-0.10 ± 0.16	0.19 ± 0.84	0.02 ± 0.18
V-band vs PD	$0.35 \pm 0.18^*$	0.05 ± 0.25	$-0.34 \pm 0.20^*$	-0.26 ± 0.14
Gamma-ray vs PD	$0.82 \pm 0.20^*$	-0.13 ± 0.22	-0.90 ± 0.58	0.11 ± 0.17
V-band vs Color (V-J)	$-0.65 \pm 0.22^*$	$-0.64 \pm 0.29^*$	-0.22 ± 0.20	$-0.56 \pm 0.48^*$

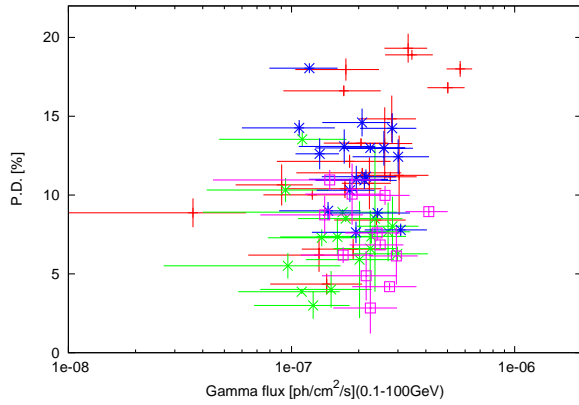


Fig. 8. Gamma-ray flux vs. optical polarization degree (PD). Colors are the same as those of Fig.6.

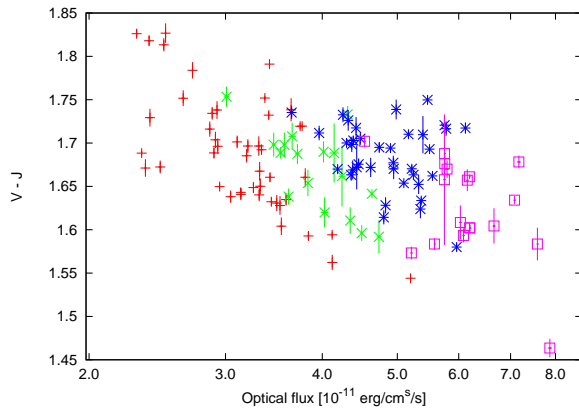


Fig. 9. Optical flux vs. color index (V-J). Colors are the same as those of Fig.6.

by VERITAS in TeV gamma rays as part of a multiwavelength campaign suggested the emission was SSC+EC based Acciari et al. 2008). On the other hand, the optical flux independently increases against the gamma-ray flux from period 1 to 4, and no clear correlation is seen between the optical and gamma-ray flux in periods 2, 3, and 4. This type of behavior is novel for 3C 66A.

The average flux in the optical and gamma-ray bands in period 1 (2008) and period 4 (2009) are listed in Table 3. The optical flux in period 4 is about twice as large as that in period 1 even though the gamma-ray flux is similar. In the framework of a one-zone picture, we assume that the jet is oriented

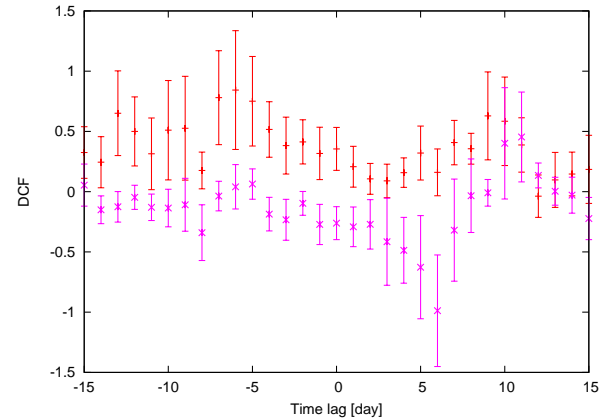
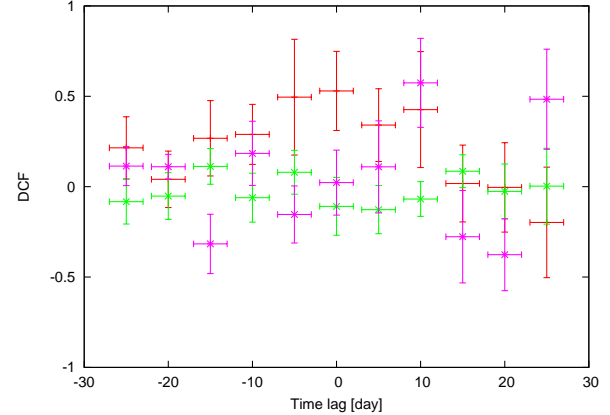


Fig. 10. Discrete correlation function (DCF) between the gamma-ray flux and optical flux (left plot), and the optical flux and PD (right plot). Colors indicate four periods; red: period 1 (MJD 54706–54831), green: period 2 (MJD 54831–55047), blue: period 3 (MJD 55047–55151), and pink: period 4 (MJD 55151–55220). The DCF in periods 2, 3 in Figure (b) are not shown because of large errors. The horizontal axis represents the time lag.

with respect to the line of sight at a very small angle so that the Doppler factor is equal to $D = (\Gamma[1 - \beta \cos \theta_{\text{obs}}])^{-1} = \Gamma$, where θ_{obs} is the angle of the jet with respect to the line of sight and $\beta = (1 - \Gamma^{-2})^{-1/2}$.

According to a simple SSC or SSC+EC scenario, if the flare is assumed to be caused by a variation of the Lorentz factor $\Gamma (=D)$, the gamma-ray peak luminosity L_{SSC} or L_{EC} is predicted to vary as $L_{SSC} \propto D^{2+\gamma}$ or $L_{EC} \propto D^{2+2\gamma}$ where γ is the photon index (Dermer et al. 1995). In an SSC or SSC+EC model, if the flare is assumed to be caused by electron input in the jet, the relation between L_{SSC} or L_{EC} and L_{sync} is expressed as, $L_{SSC} \propto L_{sync}^2$ or $L_{EC} \propto L_{sync}$ where L_{sync} is

Table 3. Average optical flux, optical color and gamma-ray flux.

Period	Optical flux [erg cm ⁻² s ⁻¹]	color (V-J)	Gamma-ray flux at 20GeV [erg cm ⁻² s ⁻¹]
period 1	(3.2 ± 0.9) × 10 ⁻¹¹	1.68 ± 0.07	(3.5 ± 1.6) × 10 ⁻¹¹
period 4	(6.0 ± 0.3) × 10 ⁻¹¹	1.62 ± 0.06	(3.8 ± 1.6) × 10 ⁻¹¹

the luminosity of the synchrotron emission of the jet. In both cases, the gamma-ray flux is expected to increase with the optical flux but our results from period 4 do not match either scenario. Since period 1 is explained by an EC model (Paper I), hereafter we only consider the EC model.

The EC radiation luminosity (L_{EC}) and synchrotron radiation luminosity (L_{sync}) are related by (Sikora et al. 2008):

$$\frac{L_{EC}}{L_{sync}} \sim \Gamma^2 \frac{u_{ext}}{u_B}. \quad (4)$$

Here, Γ is the bulk Lorentz factor of the jet, u_{ext} is the energy density of the external photons and u_B is the energy density of the magnetic field. Transforming this expression with $u_B = \frac{B^2}{8\pi}$ where B is the amplitude of magnetic field, the value of u_{ext} is then represented as

$$u_{ext} \sim \frac{B^2}{8\pi\Gamma^2} \frac{L_{EC}}{L_{sync}}. \quad (5)$$

The L_{EC}/L_{sync} ratio depends on Γ , u_{ext} and u_B . As previously discussed, the variations seen in this ratio are unlikely to be caused by variations in Γ . If variations of u_B are the reason, then B would have to be stronger in period 4. In general, the correlation between the optical flux and PD should indicate whether the magnetic field is strong, but our observations show an opposite trend. Therefore variations of u_B are unlikely. The L_{EC}/L_{sync} ratio also depends on the shape of the electron energy distribution. However, we find that the color is almost the same between periods 1 and 4 (Table 3), and thus this possibility is unlikely. Therefore, we focus on the variations of the energy density of the external photon field u_{ext} as the source of the variability. Of course there are other possible causes of the variability seen in the L_{EC}/L_{sync} ratio, such as the magnetic field and the electron energy distribution varying at the same time. In this discussion, however, we focus on only one parameter for simplicity.

We assume that the gamma-ray flux at 20 GeV, which is the peak energy of EC radiation estimated from paper I, gives a peak luminosity of the EC radiation, and also that both the optical and gamma-ray emission originates from the same region. We then calculate the energy density of external photons for periods 1 and 4. The u_{ext} in period 1 is estimated in paper I, based on fitting the multiwavelength spectra. On the other hand, it is difficult to estimate how much the EC radiation contributes to the gamma-ray emission in period 4 using only the optical and gamma-ray data. Therefore, here we assume that the gamma-ray emission is dominated by EC radiation. We roughly calculate the energy density of external photons and synchrotron photons, by using the magnetic field B , the size of the emission region R , and the jet Lorentz factor Γ in the case of redshift $z = 0.1, 0.2, 0.3, 0.444$, following Paper I. The energy density of synchrotron photons is represented as

$$u_{sync} = \frac{L_{sync}}{4\pi R^2 c D^4}. \quad (6)$$

In all cases, the u_{ext} in period 4 is about twice as that in period 1. u_{ext} can differ when the distance of the gamma-ray emission region to the seed photon source is different between periods 1 and 4. For example, if the seed photons come from the accretion disk, the distance to the central BH could be different by a factor of only 1.4 between the two periods. However, if the seed photons come from the broad-line region or the dusty torus, the situation is more complicated and beyond the scope of this work. On the other hand, the long-term correlations in the optical properties indicate the existence of two emission components which could explain the change of the L_{EC}/L_{sync} ratio.

Marscher et al. (2008) proposed a similar scenario that the radiation source consists of two or more emission regions; one a global jet region and the others a local one. In this scenario, the local emission is characterized by short-time variability (because of the small emission region) and highly polarized emission (because the small emission region aligns the magnetic field). On the other hand, the global emission consists of the addition of many local regions. We conclude that the local emission is dominant in 2008, while the global emission is dominant in 2009.

The brightening optical component in 2009 was associated with a bluer color, but the PD decreased as the flux increased. Such behavior is also found in other blazars (Ikejiri et al. 2011), and could be explained by the existence of an underlying constant component, and a short-term variable component with a different polarization direction (Uemura et al. 2010). In this case, the underlying component has a polarization with PD \sim 13 [%] and PA \sim 200 $^\circ$, while the variable component that causes the flux variation in periods 1 and 4 has a polarization whose direction is quite different. A gradual shift of PA in periods 1 and 2 supports the two-component model.

4. Summary

We performed long-term monitoring of the ISP blazar 3C 66A with the LAT onboard the *Fermi Gamma-ray Space Telescope* and the Kanata telescope and studied the correlations among various gamma-ray and optical properties. As a result, we find two distinct types of behavior: one, in 2008, which shows a correlation between the optical properties and the gamma-ray flux and the other, in 2009, which does not show a good correlation. This result indicates that the emission region is different between these periods. Paper I indicates that the emission from this source is well explained by a SSC + EC model during the 2008 flare and we estimated the environment of the jet in 2009 using same model mentioned in Paper I. Based on this assumption, we calculated the u_{ext} value in each state and found that it is different by a factor of two. Those

Table 4. Comparison of the estimated energy density of synchrotron and external photons in 2008 (period 1) and 2009 (period 4) for each redshift.

Parameter	$z = 0.1$	$z = 0.2$	$z = 0.3$	$z = 0.444$
Comoving magnetic field, B [G]	0.35	0.22	0.21	0.23
jet Lorentz factor Γ	30	30	40	50
size of blob R [10^{16} cm]	0.5	1.2	1.5	1.5
u_{sync} (period 1) [10^{-5} erg/cm ³]	10.56	8.36	4.27	4.40
u_{sync} (period 4) [10^{-5} erg/cm ³]	19.60	15.51	7.92	8.17
u_{ext} (period 1) [10^{-7} erg/cm ³]	58.61	22.98	11.78	9.04
u_{ext} (period 4) [10^{-7} erg/cm ³]	29.21	11.54	5.92	4.54

different behaviors between the gamma-ray and optical bands might be explained by postulating two different emission components.

5. Acknowledgments

The *Fermi* LAT Collaboration acknowledges generous ongoing support from a number of agencies and institutes that have supported both the development and the operation of the LAT as well as scientific data analysis. These include the National Aeronautics and Space Administration and the Department of Energy in the United States, the Commissariat à l’Energie Atomique and the Centre National de la Recherche Scientifique / Institut National de Physique Nucléaire et de Physique des Particules in France, the Agenzia Spaziale Italiana and the Istituto Nazionale di Fisica Nucleare in Italy, the Ministry of Education, Culture, Sports, Science and Technology (MEXT), High Energy Accelerator Research Organization (KEK) and Japan Aerospace Exploration Agency (JAXA) in Japan, and the K. A. Wallenberg Foundation, the Swedish Research Council and the Swedish National Space Board in Sweden.

Additional support for science analysis during the operations phase is gratefully acknowledged from the Istituto Nazionale di Astrofisica in Italy and the Centre National d’Études Spatiales in France.

This work was supported by Japan Society for the Promotion of Science (JSPS).

References

- Abdo, A. A., et al. 2010a, *ApJ*, 715, 429
 Abdo, A. A., et al. 2010b, *ApJS*, 187, 460
 Abdo, A. A., et al. 2010c, *Nature*, 463, 919
 Abdo, A. A., et al. 2010d, *ApJS*, 188, 405
 Abdo, A. A., et al. 2010e, *ApJ*, 721, 1425
 Abdo, A. A., et al. 2010f, *ApJ*, 710, 810
 Abdo, A. A., et al. 2010h, *ApJ*, 710, 1271
 Abdo, A. A., et al. 2011, *ApJ*, 726, 43
 Acciari, V. A., et al. 2008, *ApJL*, 684, 73
 Atwood, W. B., et al. 2009, *ApJ*, 697, 1071
 Bramel, D. A., et al. 2005, *ApJ*, 629, 108
 Cutri, et al. 2003, 2MASS All Sky Catalog of Point Sources, The IRSA 2MASS All-Sky Point Source Catalog, NASA/IPAC Infrared Science Archive.
<http://irsa.ipac.caltech.edu/applications/Gator/>
 Dermer C. et al. 1995, *ApJ*, 446, 63
 Edelson, R. A. & Krolik, J. H. 1998, *ApJ*, 333, 646
 Gonzalez-Perez, J. N., et al. 2001, *ApJ*, 122, 2055
 Ikejiri, Y., et al. 2011, *PASJ*, 63, 639
 Marscher, A. P., et al. 2008, *Nature*, 452, 966
 Miller, J. S., French, H. B., & Hawley, S. A. 1978, *Proc. Pittsburgh Conf. on BL Lac Objects*, ed. A. M. Wolfe,
 Nolan, P. L., et al. 2012, *ApJS*, 199, 31
 Sasada, M., et al. 2010, *PASJ*, 62, 645
 Schlegel, D., et al. 1998, *ApJ*, 500, 525
 Sikora, M., et al. 2008, *ApJ*, 675, 71
 Striani, E. et al. 2010, *ApJ*, 718, 455
 Uemura, M., et al. 2010, *PASJ*, 62, 69
 Watanabe, M., et al. 2005, *PASP*, 117, 870
 Wolff, M. J., et al. 1996, *AJ*, 111, 856
 Wright, E. L. 2006, *PASP*, 118, 1711